Icarus 338 (2020) 113509

Contents lists available at ScienceDirect

Icarus

journal homepage: www.elsevier.com/locate/icarus

Cooling patterns in rotating thin spherical shells — Application to Titan's subsurface ocean

Hagay Amit [a,*], Gaël Choblet [a], Gabriel Tobie [a], Filipe Terra-Nova [a,b], Ondřej Čadek [c], Mathieu Bouffard [d]

[a] CNRS UMR 6112, Université de Nantes, Laboratoire de Planétologie et de Géodynamique, 2 rue de la Houssinière, Nantes F-44000, France
[b] Departamento de Geofísica, Instituto de Astronomia, Geofísica e Ciências Atmosféricas, Universidade de São Paulo, Rua do Matão, 1226, Cidade Universitária, São Paulo 05508-090, Brazil
[c] Charles University, Faculty of Mathematics and Physics, Department of Geophysics, V Holešovičkách 2, Prague 18000, Czech Republic
[d] Max Planck Institute for Solar System Research, Justus-von-Liebig-Weg 3, 37077 Göttingen, Germany

A B S T R A C T

We use rotating convection simulations in a thin spherical shell to study fluid dynamics in subsurface oceans of icy moons. We find two types of persistent results, characterized by larger outer boundary heat flux either at polar regions or at the equatorial region. Simulations corresponding to larger Rossby numbers result in polar cooling with moderate lateral heterogeneity in heat flux, whereas lower Rossby numbers give equatorial cooling with more pronounced heat flux heterogeneity. The polar cooling scenario is in agreement with inferences for the heat flux at the top of Titan's ocean, which may provide a dynamical constraint for the vigor of convection in this layer. Our results may help unraveling the internal dynamics and the interactions among the different layers within the hydrosphere of Titan. Possible implications for the deep interiors of other icy moons are envisaged.

1. Introduction

Many water rich planetary bodies in the outer solar system are considered to be "ocean worlds" in the sense that these bodies likely harbor global layers of liquid water beneath their surface ice shells (cf. e. g. Nimmo and Pappalardo, 2016). Early inferences for the possible presence of internal oceans buried in distant moons relied on thermal evolution models (in the case of Jupiter's satellites Ganymede and Europa, for example, cf. Kirk and Stevenson, 1987, Ojakangas and Stevenson, 1989). Geophysical measurements by the Galileo and Cassini-Huygens missions involved various techniques for detecting buried oceans. Owing to Jupiter's detectable dipole tilt, magnetic induction enabled to identify global scale conductive layers in the major icy moons orbiting in the magnetosphere, most notably Europa (Khurana et al., 2002; Zimmer et al., 2000). For Ganymede, a more ambiguous measurement due to the presence of an internal dynamo (Kivelson and Khurana, 2002) was later confirmed by Earth-based observation of auroral oscillations (Saur et al., 2015). In the system of Saturn, evidence for internal oceans was found at three moons, Titan, Enceladus and Mimas, and internal oceans are suspected in two other moons, Dione and Rhea. For Titan, the presence of an internal ocean was confirmed by three independent observations: electric signals measured by the Huygens probe during its descent through Titan's atmosphere (Béghin et al., 2012, 2010), obliquity three times larger than expected (Baland et al., 2014, 2011) and gravitationnal tides (Iess et al., 2010; Mitri et al., 2014). For Mimas and Enceladus, the existence of a global ocean was determined from the detection of libration (Tajeddine et al., 2014; Thomas et al., 2016). For Mimas, the observed libration could also be explained by a very elongated rocky core, so that the existence of an ocean is not certain (Tajeddine et al., 2014). In the case of Enceladus, the existence of a global ocean is also consistent with the observed topography and graviy fields (Beuthe et al., 2016; Čadek et al., 2016; Hemingway et al., 2018). Such oceans constitute at present some of the most promising of potentially habitable extraterrestrial environments and two ambitious planetary missions to come are devoted to their characterization: ESA's JUICE scrutinizing Ganymede (Grasset et al., 2013) and NASA's Europa Clipper (Phillips and Pappalardo, 2014).

Observations of non-water compounds at Europa's surface (Ligier et al., 2016; McCord et al., 2002) and in ejected icy grains at Enceladus (Hsu et al., 2015, 2018; Postberg et al., 2009, 2011) suggest chemical transport from the ocean seafloor up to the surface. However, the practical means by which the oceans convey this signature are uncertain. Convection in Europa's buried ocean was considered in the light of localized heating at its seafloor in a weakly stratified ocean (Thomson

* Corresponding author.
E-mail address: Hagay.Amit@univ-nantes.fr (H. Amit).

https://doi.org/10.1016/j.icarus.2019.113509
Received 25 March 2019; Received in revised form 27 September 2019; Accepted 26 October 2019
Available online 9 November 2019
0019-1035/© 2019 Elsevier Inc. All rights reserved.

and Delaney, 2001). Their scaling analysis of rotationally confined instabilities is further constrained by dedicated experiments (Goodman et al., 2004). Vance and Goodman (2009) set such mechanisms in the more general context of an uncertain Europan oceanography, including global scale convecting and rotating flow. Double diffusive convection is also envisioned (Vance and Brown, 2005).

Although often with a thick shell in the context of Earth's outer core, the pattern of convection and heat transport in rapidly rotating spherical shells at onset and their dependence on control parameters have been thoroughly explored (for a review see e.g. Aurnou et al., 2015). Dormy et al. (2004) identified the onset of convection at the edge of the tangent cylinder for any spherical shell thickness. Zhang and Jones (1993) found that an Ekman boundary layer that is formed where axial convective rolls impinge the outer boundary destabilizes/stabilizes convection when viscous/thermal dissipation dominates, respectively. Tilgner and Busse (1997) observed that when convection vigor is enhanced the heat transport across the shell increases, in particular at polar regions. Gastine et al. (2016) conducted a systematic parametric study of convection in a rotating spherical shell of aspect ratio 0.6. They established scaling laws that separate different convective regimes.

Soderlund et al. (2014) modelled rotating convection in a thin 3D spherical shell for a subsurface ocean. They found latitudinal dependence of heat transfer. In the case of Europa, this effect may explain the preferred occurrence of specific surface features (chaos terrains, salt deposits) at moderate latitudes. In thin, rapidly rotating ocean shells the outer boundary heat flux is expected to be concentrated at low latitudes (Miquel et al., 2018). Other efforts to relate the global ice shell structure of ocean worlds to ocean dynamics have focused on ice shell melting, e.g. in the case of Europan chaos-type features (Thomson and Delaney, 2001), Titan (Kvorka et al., 2018) or Enceladus (Čadek et al., 2019), but the possible lessons on ocean dynamics and heat transfer are only preliminary.

In this context, we follow the approach initiated by Soderlund et al. (2014) to better characterize the dynamics of buried oceans at a global scale. We present simulations of thermal convection of a rotating fluid in a thin spherical shell for a range of control parameters. We focus on the resulting heat flux pattern at the top of the shell. Due to computational limitations (e.g. Glatzmaier, 2002) the explored control parameters are very remote from the actual values in buried oceans — some projections of our results thus require extrapolation (as is the case for most rapid rotation applications, cf. Aubert et al., 2017).

The paper is outlined as follows. In Section 2, we detail our method. Our results are analyzed in Section 3. We place our models in the expected dynamical regime based on previous literature (Section 4) and then compare the results from our simulations to inferences from Cassini's observations for the heat flux at the top of Titan's ocean (Section 5). Finally, we discuss the main results and their implications for Titan's ocean (Section 6).

2. Method

We simulate rotating convection in a thin spherical shell. The impact of the shell thickness on the convection style is not trivial. In the case of rapidly rotating models, Miquel et al. (2018) found that the determining parameter to characterize the vigor and extent of low-latitude convective trapping combines the geometry and rotational effects. When thermal forcing is enhanced, convection emerges inside the tangent cylinder (e.g. Tilgner and Busse, 1997); hence, the shell thickness which dictates the surficial extent of the tangent cylinder becomes an important factor. Deep liquid systems encompass a variety of shell thicknesses. In Table 1, we list the shell thicknesses and the corresponding relative tangent cylinder surfaces of some of these systems. Here, we term a shell "thin" as one that its inner to outer radii ratio r_i/r_o is significantly larger than e.g. that of Earth's outer core resulting in a relative tangent cylinder surface about an order of magnitude larger than that of Earth's outer core.

Table 1
Deep liquid systems, their aspect ratio and relative tangent cylinder surface. Ranges for Mercury's core are based on combinations of the first and third quartiles of Hauck et al. (2018), see their Table 5. For comparison we give the values for our models in the last line.

System	r_i/r_o	S^h/S	Reference
Mercury's core	0.15 – 0.50	0.01 – 0.13	Hauck et al. (2018)
Earth's core	0.35	0.06	Dziewonski and Anderson (1981)
Titan's ocean	0.84 – 0.96	0.46 – 0.72	Vance et al. (2018)
Enceladus' ocean	0.78 – 0.90	0.37 – 0.56	Čadek et al. (2019)
Europa's ocean	0.92 – 0.94	0.61 – 0.66	Vance et al. (2018)
Pluto's ocean	0.94	0.66	Gabasova et al. (2018)
Our models	0.8	0.4	

The numerical models solve the following set of self-consistent non-dimensional Boussinesq hydrodynamics equations for thermal convection of a fluid in a rotating spherical shell:

$$E\left(\frac{\partial \vec{u}}{\partial t} + \vec{u}\cdot\nabla\vec{u} - \nabla^2\vec{u}\right) + 2\hat{z}\times\vec{u} + \nabla P = Ra^*\frac{\vec{r}}{r_o}T \tag{1}$$

$$\frac{\partial T}{\partial t} + \vec{u}\cdot\nabla T = \frac{1}{Pr}\nabla^2 T \tag{2}$$

$$\nabla\cdot\vec{u} = 0, \tag{3}$$

where $\vec{u}$ is velocity, T is temperature, t is time, $\hat{z}$ is a unit vector in the direction of the rotation axis, P is pressure and $\vec{r}$ is position vector. Three non-dimensional parameters in Eqs. (1)– (3) control the dynamics. The modified Rayleigh number Ra^* represents the strength of buoyancy force driving the convection relative to retarding forces

$$Ra^* = \frac{\alpha g_0 \Delta T D}{\nu\Omega}, \tag{4}$$

where α is thermal expansivity, g_0 is gravitational acceleration on the outer boundary at radius r_o, ΔT is the fixed temperature difference between the inner and outer boundaries, D is shell thickness, ν is kinematic viscosity and Ω is the rotation rate. The Ekman number represents the ratio of viscous and Coriolis forces

$$E = \frac{\nu}{\Omega D^2}. \tag{5}$$

The Prandtl number is the ratio of kinematic viscosity to thermal diffusivity

$$Pr = \frac{\nu}{\kappa}, \tag{6}$$

where κ is thermal diffusivity. The modified Rayleigh number Ra^* is related to the conventional Rayleigh number by $Ra^* = Ra \cdot E/Pr$, where the conventional Rayleigh number Ra is given by

$$Ra = \frac{\alpha g_0 \Delta T D^3}{\nu\kappa}. \tag{7}$$

To dimensionalize the solutions velocity is scaled by D/ν, time by D^2/ν and temperature by ΔT.

Some relevant output parameters are monitored. The Reynolds number which represents the ratio of inertial to viscous forces is calculated based on the rms velocity U in the volume of the shell

$$Re = \frac{UD}{\nu} \tag{8}$$

and the Rossby number represents the ratio of inertial to Coriolis forces

$$Ro = \frac{U}{\Omega D} = Re\cdot E. \tag{9}$$

The magnitude of the heat flux anomaly on the outer (or inner) boundary q_o^* (or q_i^*) is defined as the ratio of the peak-to-peak amplitude of the zonal part of the heat flux to twice the mean heat flux:

$$q^* = \frac{q^z_{\max} - q^z_{\min}}{2q_0}, \tag{10}$$

where z superscript corresponds to "zonal", i.e. averaging over latitude lines. This definition differs from the more common definition based on the 2D heat flux distribution and applied to large-scale input patterns (e.g. Olson and Christensen, 2002), while alternative definitions were used for localized patterns (for a review see Amit et al., 2015). Here, we use the zonal heat flux in order to avoid bias from small-scale longitudinal variability which might arise solely due to the finite simulation time of the runs.

The tangent cylinder effect is also quantified. We calculate the normalized difference between the time-average outer boundary heat flux inside to outside the tangent cylinder as follows:

$$< q_o >^{h/l} = \frac{< q_o >^h - < q_o >^l}{< q_o >^h + < q_o >^l}, \tag{11}$$

where the mean heat flux inside the tangent cylinder, denoted by h superscript (for higher latitudes), is

$$< q_o >^h = \frac{1}{2S^h}\left(\int_0^{2\pi}\int_0^{\theta_{tc}} q_o(\phi,\theta)dS + \int_0^{2\pi}\int_{\pi-\theta_{tc}}^{\pi} q_o(\phi,\theta)dS \right) \tag{12}$$

and the mean heat flux outside the tangent cylinder, denoted by l superscript (for lower latitudes), is

$$< q_o >^l = \frac{1}{S^l}\int_0^{2\pi}\int_{\theta_{tc}}^{\pi-\theta_{tc}} q_o(\phi,\theta)dS. \tag{13}$$

In Eqs. (12) –(13), S^h and S^l are the outer boundary spherical surface areas inside and outside the tangent cylinder respectively, θ_{tc} is the co-latitude where the tangent cylinder intersects the outer boundary in the northern hemisphere given by $\sin\theta_{tc} = r_i/r_o$ and the spherical surface increment is $dS = r^2\sin\theta d\phi d\theta$ (for a schematic illustration see Fig. 1). The ratio $< q_o >^{h/l}$ (Eq. (11)) has some desired properties. For polar/equatorial cooling, it is positive/negative respectively, i.e. its sign indicates which cooling dominates. In addition, if one of the two coolings is much stronger $< q_o >^{h/l}$ will approach ± 1 whereas if the two coolings are comparable it will approach zero, i.e. its magnitude reflects the amplitude of the tangent cylinder effect.

The transition to a more turbulent regime may be marked by different non-dimensional numbers (see Soderlund et al., 2014, and references therein). Apart from the conventional Rossby number Ro (Eq. (9)), alternatives include the convective Rossby number

$$Ro_c = \left(\frac{RaE^2}{Pr}\right)^{1/2}, \tag{14}$$

the local convective Rossby number

$$Ro_{loc} = Ra^{5/4}E^2 \tag{15}$$

and a ratio representing a competition between thermal and rotational boundary layers

$$Ra/Ra_T = 0.1RaE^{3/2} \tag{16}$$

where Ra_T is a transitional Rayleigh number in water.

We use the code MAGIC by Johannes Wicht (Wicht, 2002). We analyze hydrodynamic (i.e. non-magnetic) models with rigid isothermal boundary conditions. We focus on the dynamics in relatively thin shells which are relevant for subsurface oceans of icy satellites. A summary of model control parameters, geometries and some output parameters is given in Table 2.

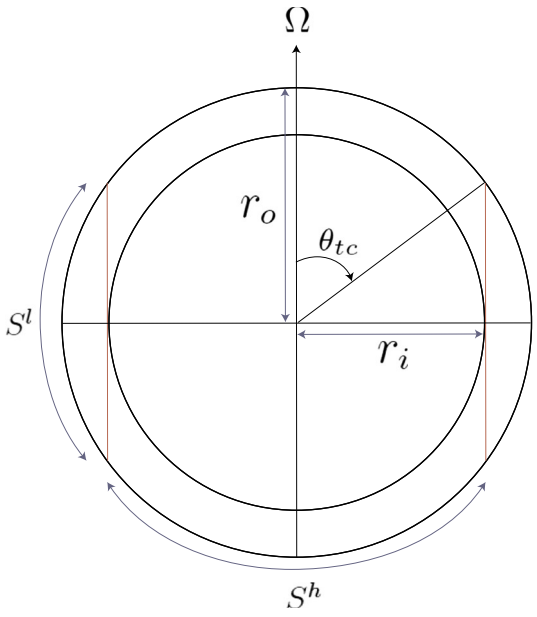

Fig. 1. Schematic illustration of the tangent cylinder geometry. The rotation rate Ω denotes the rotation axis, the horizontal line is the equatorial plane, red vertical lines denote the tangent cylinder. r_i and r_o are the inner and outer radii, respectively, θ_{tc} is the co-latitude where the tangent cylinder intersects the outer boundary in the northern hemisphere, S^h and S^l are the outer boundary spherical surface areas inside and outside the tangent cylinder, respectively (represented by arcs in this schematic cross-section). (For interpretation of the references to color in this figure legend, the reader is referred to the web version of this article.)

Note that our control parameters are far from being realistic due to computational limitations (e.g. Glatzmaier, 2002). In particular, the Ekman number in our models is far too large. Recent geodynamo simulations have reached significantly smaller Ekman numbers (Aubert et al., 2017; Schaeffer et al., 2017), though limited to relatively short runs. Our choice of larger E values allows for sufficiently long simulations characterized by decent statistical convergence towards meaningful time-average patterns. In addition, as we will show in the next section, despite the relatively larger Ekman numbers our models cover the two endmember patterns of the outer boundary heat flux.

3. Results

Fig. 2 shows some images from an arbitrary snapshot of the large-scale case 1. Despite the large Ekman number, the moderate Rayleigh number leads to dynamics that is nevertheless affected by rotational effects. In our models, convection is organized in equatorially symmetric axial columns (e.g. Busse, 1970, Taylor, 1917). This is evident in the form of north-south elongated radial vorticity (Fig. 2b) and heat flux (Fig. 2d) structures just below and on the outer boundary respectively, which result from deep meridional flow structures that are parallel to the rotation axis (Fig. 2c). The inner/outer radii ratio of 0.7 corresponds to a tangent cylinder intercepting the outer boundary at latitudes 46°. Indeed, the north-south elongated outer boundary heat flux and radial vorticity structures extend until about this latitude, while at higher latitudes convection is weaker. The axial convective columns and the tangent cylinder signature testify for the influence of rotation in the dynamics of this model.

Fig. 3 shows the same images for a long-term time-average of the same case. As expected, time-averaging smooths most of the small-scale longitudinal variability. The axial invariance of the flow (Fig. 3c) and the tangent cylinder effect (Fig. 3b) are clearly evident. The outer boundary heat flux is larger/lower at the equator/poles respectively

Table 2
Summary of models. The critical Rayleigh number Ra_c was obtained using the open-source eigenmode solver Singe (Schaeffer, 2013; Vidal and Schaeffer, 2015), available at https://bitbucket.org/nschaeff/singe. In all cases, $Pr = 1$. The maximum spherical harmonic degree and order is ℓ_{max} and the number of radial grid points in the shell is n_r. The duration of the simulations is given in units of advection time. Other control and output parameters are defined in the text.

Case	r_i/r_o	E	Ra	Ra/Ra_c	ℓ_{max}	n_r	Ro_c	Ro_{loc}	Ra/Ra_T	Re	Ro	Duration
1	0.7	$1 \cdot 10^{-3}$	$2 \cdot 10^5$	6.28	64	49	0.45	4.2	0.63	40	0.040	73
2	0.8	$1 \cdot 10^{-3}$	$2 \cdot 10^5$	7.80	64	49	0.45	4.2	0.63	48	0.048	45
3	0.8	$1 \cdot 10^{-3}$	$1 \cdot 10^6$	38.99	64	49	1	31.6	3.2	170	0.170	58
4	0.8	$1 \cdot 10^{-3}$	$3 \cdot 10^6$	116.96	64	49	1.7	124.9	9.5	335	0.335	52
5	0.8	$3 \cdot 10^{-4}$	$1 \cdot 10^6$	9.79	64	49	0.30	2.8	0.52	104	0.031	37
6	0.8	$3 \cdot 10^{-4}$	$1 \cdot 10^7$	97.85	64	49	0.95	50.6	5.2	523	0.157	36
7	0.8	$3 \cdot 10^{-4}$	$5 \cdot 10^7$	489.26	64	49	2.1	378.4	26.0	1273	0.382	35
8	0.8	$1 \cdot 10^{-4}$	$1 \cdot 10^7$	26.09	96	49	0.32	5.6	1	375	0.038	110
9	0.8	$1 \cdot 10^{-4}$	$2 \cdot 10^7$	52.18	96	49	0.45	13.4	2	638	0.064	94
10	0.8	$1 \cdot 10^{-4}$	$5 \cdot 10^7$	130.46	96	49	0.71	42.0	5	1140	0.114	98
11	0.8	$5 \cdot 10^{-5}$	$1 \cdot 10^7$	11.13	96	61	0.16	1.4	0.35	376	0.019	57

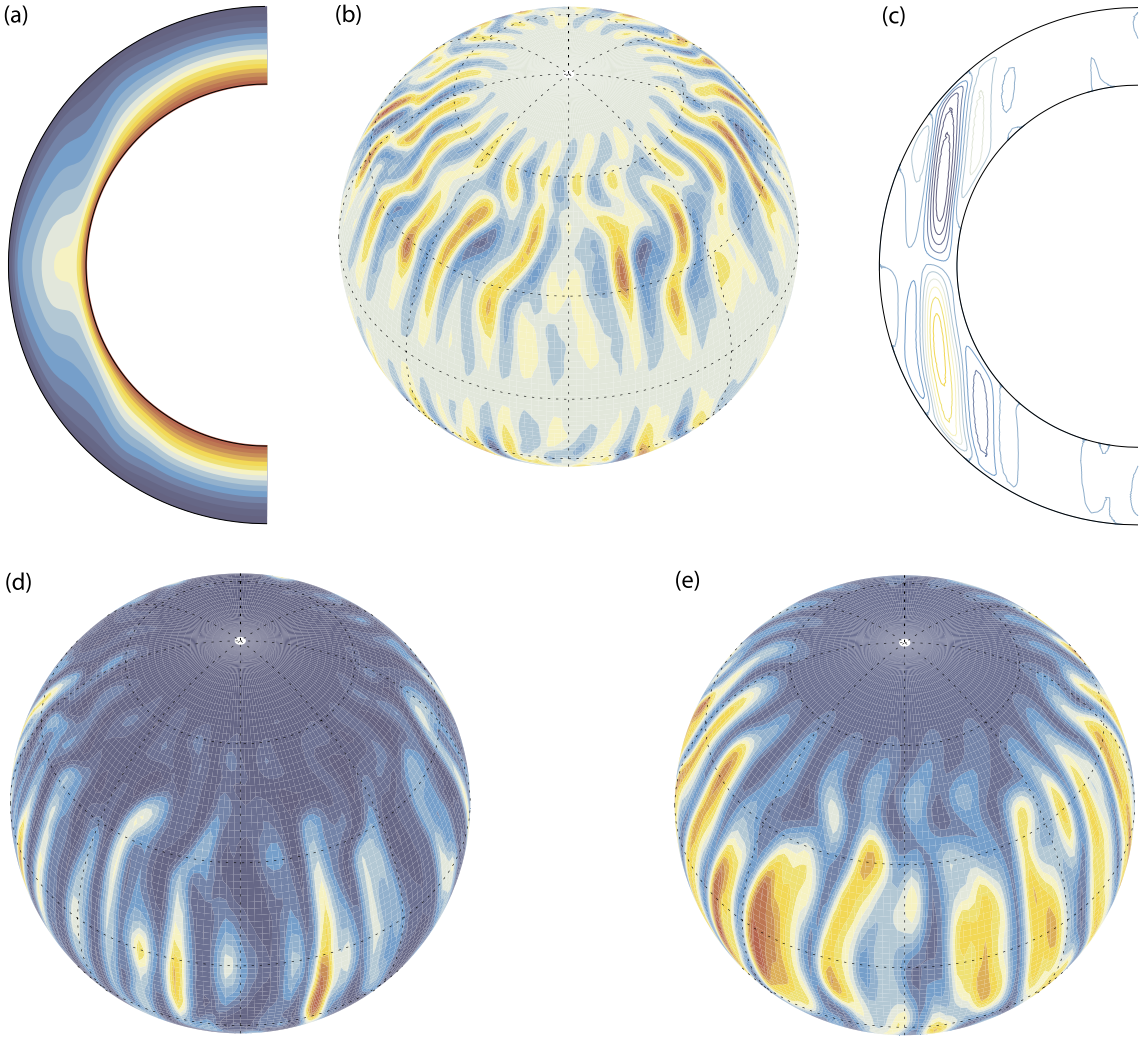

Fig. 2. Images from a snapshot of case 1. (a) Zonally-averaged temperature; (b) Radial vorticity just below the outer boundary layer; (c) Streamlines of the zonally-averaged meridional flow; (d) Heat flux across the outer boundary; And (e) heat flux across the inner boundary. In (a) red/blue denotes hot/cold respectively. In (b) red/blue denotes positive/negative radial vorticity, i.e. anti-clockwise/clockwise circulation, respectively. In (c) red/blue contours denote anti-clockwise/clockwise circulation, respectively. In (d) and (e) red/blue denote positive/negative heat flux anomaly (i.e. heat flux with respect to the mean), respectively. (For interpretation of the references to color in this figure legend, the reader is referred to the web version of this article.)

(Fig. 3d), which we term "equatorial cooling" (following Heimpel and Evans, 2013).

The corresponding instantaneous and time-average distributions of inner boundary heat flux anomalies are given in Figs. 2e and 3e, respectively. The inner boundary heat flux anomaly is also positive at low-latitudes and negative at high-latitudes. The axial columnar flow touches the inner boundary in the equatorial plane and it is there where the heat is most effectively extracted from the inner boundary (Aubert et al., 2008). The approximately spherical harmonic Y_2^0 pattern is especially prominent in the time-average map (Fig. 3e). The same time-

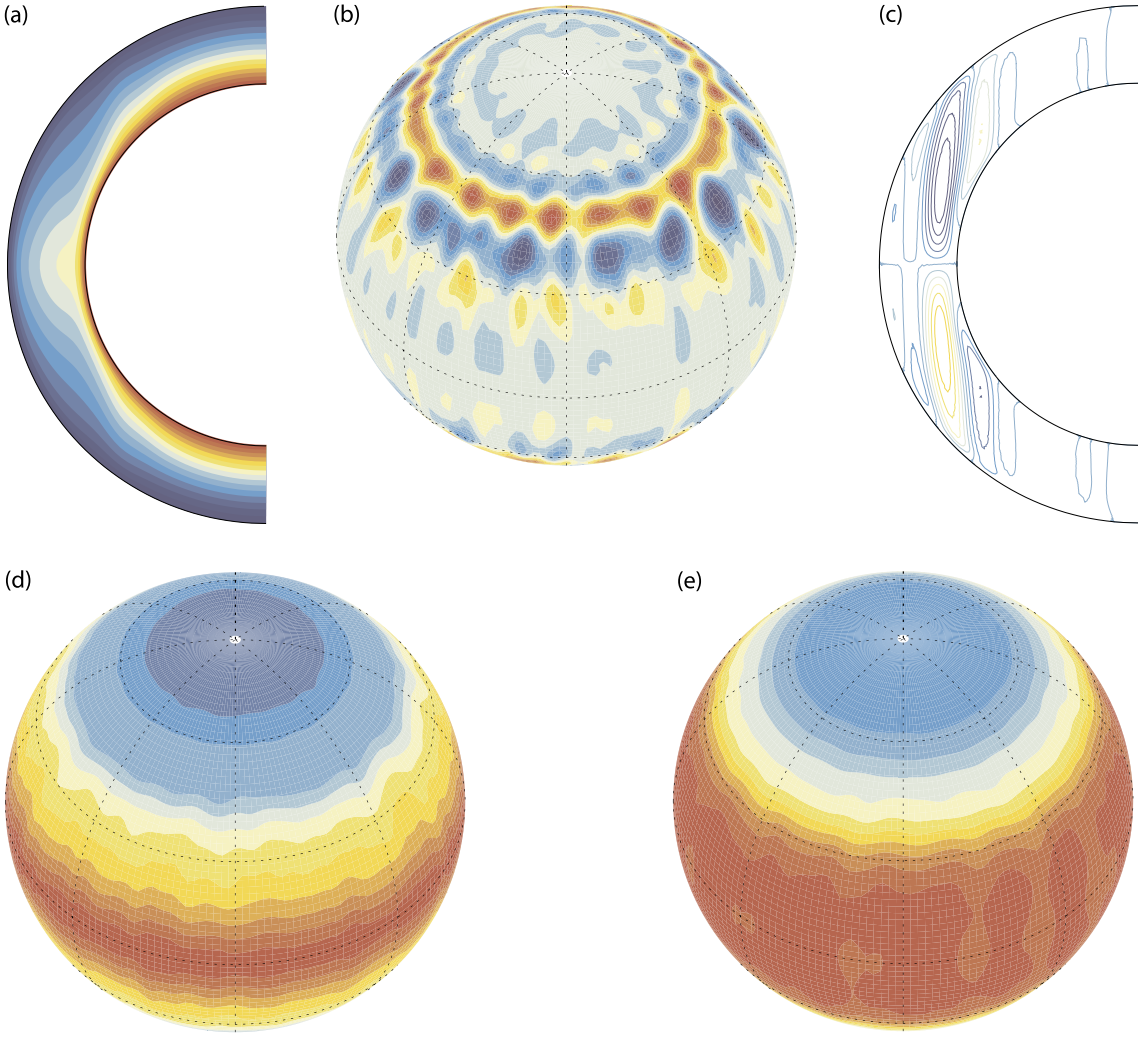

Fig. 3. As in Fig. 2 for a long-term time-average of case 1, an example of equatorial cooling.

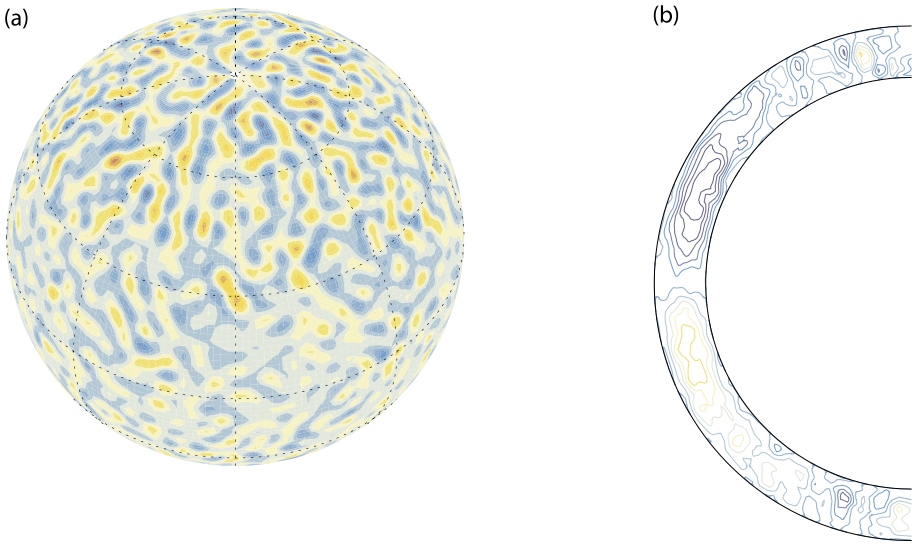

Fig. 4. Images from a snapshot of case 10. (a) Radial vorticity just below the outer boundary layer; (b) Zonally-averaged meridional flow. Red/blue denotes anti-clockwise/clockwise circulation, respectively. (For interpretation of the references to color in this figure legend, the reader is referred to the web version of this article.)

average Y_2^0 pattern was also found in numerical dynamo simulations with Earth-like core geometry and a somewhat different convection style (Amit and Choblet, 2009; Aubert et al., 2008). From hereafter, we focus on the time-average heat flux on both boundaries.

Rotational effects can be observed for a thinner shell as well. In all other cases the inner/outer radii ratio is increased to 0.8. In this geometry, the tangent cylinder intercepts the outer boundary at lower latitudes, 37° in these cases. In addition, for the same control parameters, convection is slightly stronger when confined to a thinner shell, resulting in a higher Reynolds number (compare cases 1 and 2 in Table 2) and thinner axial columns of instantaneous flow (not shown).

When convection is significantly stronger, the role of inertia in the dynamics may become more important. In cases 9–10, the Rayleigh number is more than a hundred times larger than in case 1. This results in a much larger *Re* and a larger *Ro* values (see Table 2) that characterize a more turbulent flow. The instantaneous axial convective rolls seen in case 1 (Figs. 2b and c) are broken and convective plumes fill the entire shell including inside the tangent cylinder (Fig. 4). The time-average outer boundary heat flux anomalies also exhibit a Y_2^0 pattern as in case 1, but perhaps surprisingly with an opposite sign (Fig. 5a), which we term "polar cooling".

An intermediate cooling scenario is found in case 8. The outer boundary heat flux anomaly is largest at the equator but also peaks at high latitudes with minima at mid latitudes, resembling spherical harmonic Y_4^0 rather than Y_2^0 (Fig. 6a). We term this more complicated latitudinal dependence "intermediate cooling" (Table 3).

Figs. 3, 5 and 6 demonstrate that the runs are long enough to remove most of the transient longitude-dependent features from the time-average patterns. This allows evaluating the results in terms of their zonal profiles (Fig. 7). Comparing cases 1 and 2 which have the same control parameters except for the shell thickness (Table 2), although the convective power depends on both *Ra* and the shell thickness (e.g. Aubert et al., 2009), the tangent cylinder is distinguishable between the two zonal outer boundary heat flux patterns. In case 1, a change of trend appears at higher latitudes (close to the dashed vertical line denoting the tangent cylinder in case 1), whereas in case 2, a change of trend appears at lower latitudes (close to the dotted vertical line denoting the tangent cylinder in case 2). In these cases, equatorial cooling prevails (Fig. 7 left and Table 3). Note the change of trend in the latitudinal dependence of the heat flux in both cases, from steep outside to more moderate inside the tangent cylinder. The other equatorial cooling cases 5 and 11 conform to this behavior as well, with the latter exhibiting the strongest dichotomy between a peak equatorial to low polar heat flux (Fig. 7 left and Table 3). Opposite trends characterize the polar cooling cases, with steep variation inside the tangent cylinder and rather flat heat flux outside it (Fig. 7 right and Table 3). Overall, the change in trend appears at somewhat lower latitudes than that of the tangent cylinder. Finally, the intermediate case 8 does not fall into any of the two categories (Fig. 7 middle and Table 3).

Table 3 and Figs. 8– 9 summarize the results in terms of the parameter dependence of the time-average mean heat flux, time-average amplitudes of heat flux heterogeneities and the tangent cylinder effect. The mean outer and inner boundary heat fluxes generally increase with increasing Ro_{loc} (Fig. 8a) as well as when other theoretical forms of the Rossby number increase (Fig. 9a). This is expected because increasing *Ra* leads to faster flow, larger inertial effects and consequently larger heat flux. Note that polar cooling (triangles) is characterized by larger mean heat flux than equatorial cooling (diamonds). Around $Ro_{loc} \sim 5$–10 (or corresponding critical values of *Ro*, Ro_c and Ra/Ra_T), the pattern shifts from equatorial cooling for smaller values to polar cooling for larger values. In addition, decreasing inertia results in decreasing heat flux spatial variability, i.e. polar cooling is characterized by lower (relative) heat flux heterogeneities whereas equatorial cooling is characterized by larger heat flux heterogeneities (Figs. 8b and 9b). This result is expected because when *Ro* is increased the models approach the non-rotating regime in which the heat flux is homogeneous. Also note that for both polar and equatorial coolings, the amplitude of the outer boundary heat flux heterogeneity (black) is slightly larger than that of the inner boundary (red).

The magnitude of the tangent cylinder effect, measured by Eq. (11), is shown in Figs. 8c and 9c. For polar cooling, the effect is weakly dependent on the control parameters, with a tendency to converge to zero as the relative effect of rotation decreases on approach to the non-rotating regime. In contrast, for equatorial cooling, the tangent cylinder effect is stronger with the magnitude of $< q_o >^{h/l}$ steadily decreasing with increasing inertia, reflecting the transition from dominance of axial convective rolls outside the tangent cylinder for the lowest Rossby numbers to more turbulent conditions in the larger Rossby numbers. The largest tangent cylinder effect with polar cooling is registered in case 9 with $< q_o >^{h/l} = 0.16$, whereas in case 11 with equatorial cooling $< q_o >^{h/l} = -0.47$ (Table 3). The latter case with the lowest Ekman number (Table 2) also exhibits the largest (relative) heterogeneity (Figs. 8– 9).

In most cases, the inner boundary heat flux shows a similar cooling pattern as the outer boundary heat flux, i.e. either polar cooling or equatorial cooling prevails in both (Table 3). However, this is not always precisely the case (see e.g. Fig. 6). In cases 7 and 10, polar cooling prevails on the outer boundary whereas the inner boundary is more small scale with a peak at mid latitudes vs. minima at the equator and the poles (which we classify as "mid latitudes" in Table 3), while in case 6 again polar cooling is observed on the outer boundary whereas the inner boundary is characterized by polar peak, equatorial low, but in addition low-latitude peaks (which we classify as "quasi polar" in Table 3). Overall, a nearly z-invariant convection pattern is not expected to produce correlated heat flux patterns in the two boundaries, and such

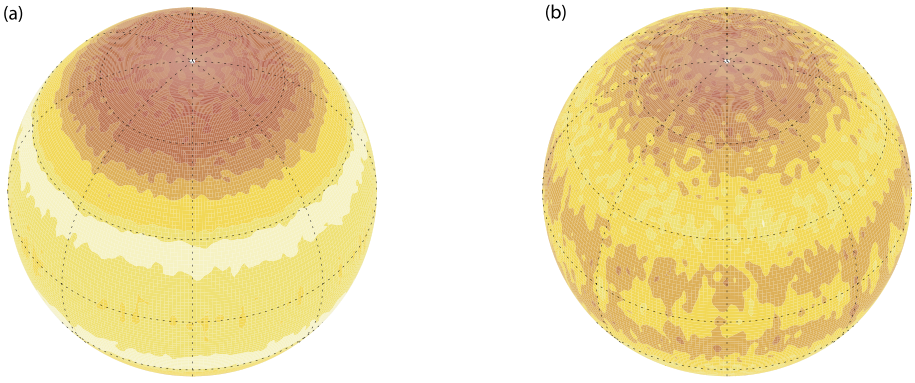

Fig. 5. Heat fluxes for a long-term time-average of case 9, an example of polar cooling. (a) Across the outer boundary; (b) Across the inner boundary. Red/blue denote positive/negative heat flux anomaly (i.e. heat flux with respect to the mean), respectively. (For interpretation of the references to color in this figure legend, the reader is referred to the web version of this article.)

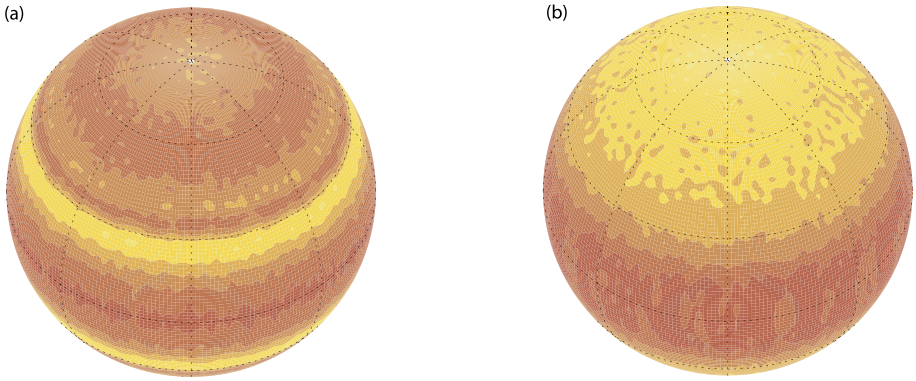

Fig. 6. As in Fig. 5 for case 8, with intermediate cooling.

Table 3
Time-average cooling patterns and amplitudes. Positive anomaly of equatorial/polar outer boundary heat flux is termed "Equatorial cooling"/"Polar cooling" respectively. Other quantities are defined in the text.

Case	$< q_o >$	$< q_i >$	Outer cooling	$< q_o >^{h/l}$	Inner cooling	$< q_o^* >$	$< q_i^* >$
1	1.69	3.44	Equatorial	− 0.39	Equatorial	0.59	0.46
2	2.40	3.75	Equatorial	− 0.19	Equatorial	0.37	0.32
3	5.89	9.20	Polar	0.13	Polar	0.22	0.09
4	8.68	13.55	Polar	0.08	Polar	0.15	0.06
5	3.52	5.50	Equatorial	− 0.23	Equatorial	0.46	0.45
6	11.02	17.21	Polar	0.11	Quasi-polar	0.21	0.04
7	18.34	28.60	Polar	0.06	Mid latitudes	0.12	0.07
8	7.99	12.49	Intermediate	0.02	Equatorial	0.16	0.17
9	12.17	19.00	Polar	0.16	Polar	0.26	0.07
10	17.10	26.68	Polar	0.13	Mid latitudes	0.21	0.05
11	4.33	6.76	Equatorial	− 0.47	Equatorial	0.91	0.83

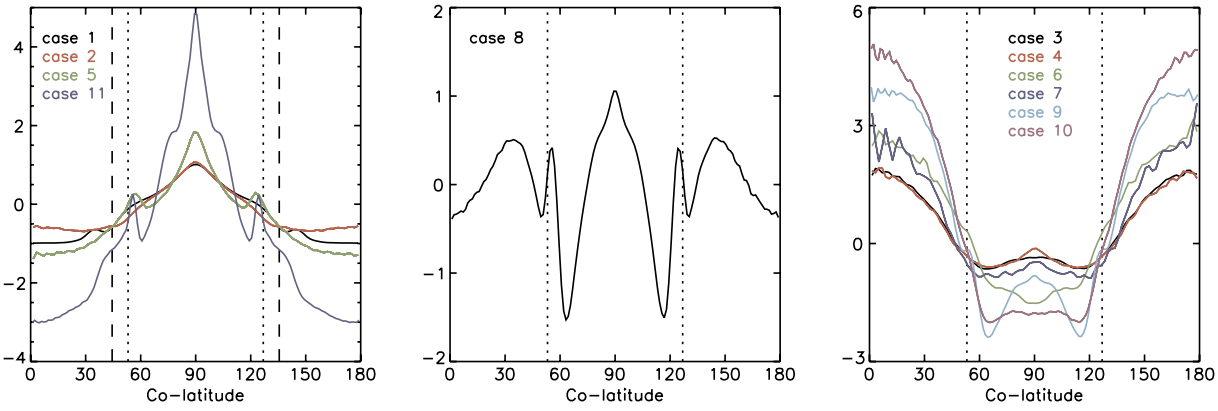

Fig. 7. Non-dimensional zonally-averaged outer boundary heat flux anomalies for the long-term time-averages of equatorial cooling cases (left), the intermediate cooling case 8 (middle) and polar cooling cases (right). The dashed vertical lines (left) denote the latitudes of the tangent cylinder in case 1, the dotted vertical lines denote the latitudes of the tangent cylinder in the other cases. Note the different scales.

similarities probably arise due to thermal diffusion effects in the simulated thin shell. In realistic planetary conditions these diffusive effects are expected to be smaller (Aubert et al., 2007). Overall, the outer boundary heat flux seems to globally display larger scale patterns than the inner boundary heat flux.

4. Dynamical regime for buried oceans

Here, we introduce possibly relevant parametric regimes. Fig. 10 presents the regime diagram of Gastine et al. (2016) (dashed grey curves) for convecting rotating flows in a spherical shell. The regime diagram is given in terms of the Ekman and Rayleigh numbers. At the onset of supercritical convection, the flow is weakly non-linear. When the Rayleigh number exceeds six times the critical value for convection, three flow regimes are possible. For small Rayleigh numbers such that $Ra < 0.4E^{-8/5}$, the flow resides in a rapidly rotating regime. For strongly convecting systems in which $Ra > 100E^{-12/7}$, the flow is in a non-rotating regime. In between, a transitional regime prevails. For more details, see Gastine et al. (2016).

We consider Titan's ocean as an emblematic example for our models (see Section 5). In order to estimate the appropriate Ekman and Rayleigh numbers for Titan's ocean, we adopt the models by Vance et al. (2018) to constrain its geometry. The extreme values for thickness, $D = 91$ km (ocean with 10% $MgSO_4$, densest core) and 420 km (ocean with pure water, less dense core), lead respectively to $r_i/r_o = 0.96$ and 0.84. Assuming a viscosity $\nu = 1.8 \cdot 10^{-6}\,\mathrm{m^2\,s^{-1}}$ and a given rotation rate

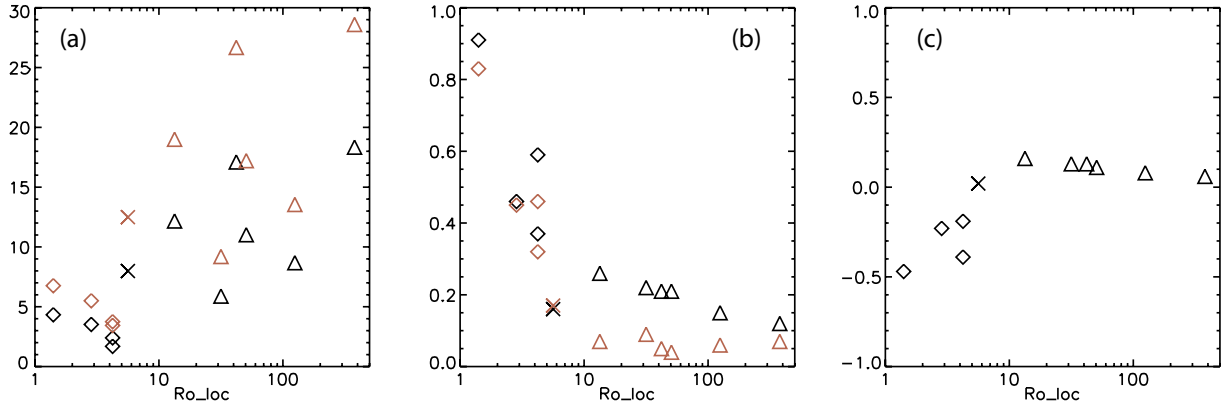

Fig. 8. (a) Time-average non-dimensional mean outer boundary heat flux $< q_o >$ (black) and inner boundary heat flux $< q_i >$ (red), (b) amplitudes of the time-average outer boundary heat flux heterogeneity $< q_o^* >$ (black) and inner boundary heat flux heterogeneity $< q_i^* >$ (red), and (c) normalized difference between inside to outside tangent cylinder outer boundary heat flux, all as functions of the local convective Rossby number Ro_{loc} (Eq. (15)) in semi-log scale. Equatorial cooling is denoted by diamonds, polar cooling by triangles and intermediate cooling (case 8) by Xs. Note that the classification of symbols is based on the outer boundary heat flux patterns. (For interpretation of the references to color in this figure legend, the reader is referred to the web version of this article.)

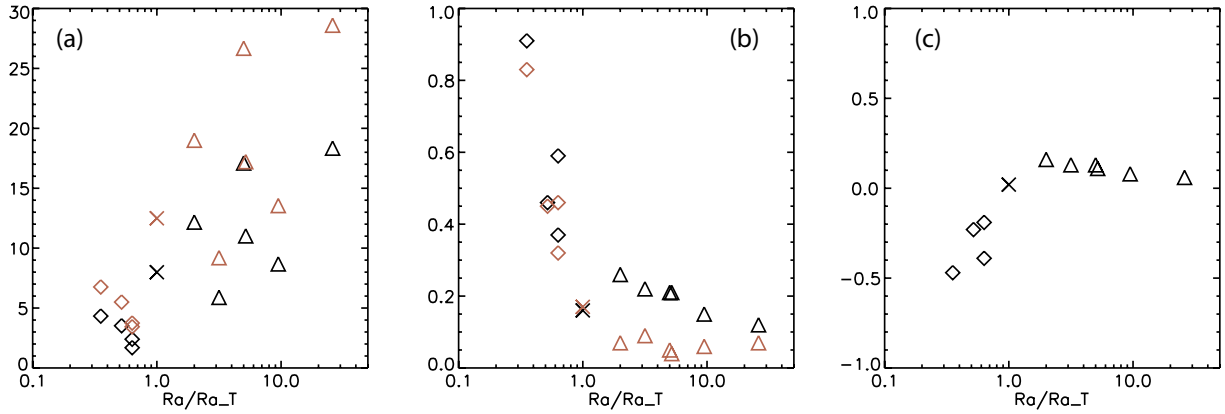

Fig. 9. As in Fig. 8 but as functions of Ra/Ra_T (Eq. (16)).

$\Omega = 4.6 \cdot 10^{-6}\,s^{-1}$ at present, this range of values for D leads to a relatively robust range for the Ekman number $E = 1.9 \cdot 10^{-12}$–$4.8 \cdot 10^{-11}$.

Estimates of the Rayleigh number for Titan's ocean are much less well constrained as it further depends on other thermodynamical constants and crucially on the essentially unknown temperature difference across the ocean ΔT. This temperature difference can be derived from the Nusselt-Rayleigh relation and an estimate of the heat flux at the top of the ocean, q_o. The Nusselt number is defined as:

$$Nu = \frac{q_o D}{\rho C_p \kappa \Delta T}. \tag{17}$$

The extrapolation of *Nu–Ra* relation to very high Rayleigh numbers is, however, debatable (e.g. Gastine et al., 2015; Roche et al., 2010). To obtain the Nusselt and Rayleigh numbers relevant for Titan's ocean, we first use two estimates of *Nu–Ra* relation proposed earlier for the non-rotating regime: $Nu = 0.07 \cdot Ra^{1/3}$ and $Nu \propto Ra^{0.389}$, derived from numerical simulations (Gastine et al., 2015, cyan dashed lines in Fig. 10) and laboratory experiments (Roche et al., 2010, blue dashed lines in Fig. 10) respectively. In particular, Roche et al. (2010) showed that the Ra exponent increases for $Ra > 7 \cdot 10^{11}$, a regime that cannot be reached in numerical simulations, from 0.33 to 0.389. For the second power law we obtain a prefactor 0.0171 by assuming that the two laws predicted the same Nusselt number for a Rayleigh number equal to 10^{11}, i.e. $Nu = 0.0171 \cdot Ra^{0.389}$. We also consider the scaling relation corresponding to rapidly-rotating convection (Gastine et al., 2016): $Nu = 0.15 Ra^{3/2} E^2$ (green dashed lines in Fig. 10).

Thermal evolution models predict that the power coming out of the rocky core of Titan at present is between 450 and 600 GW (Tobie et al., 2006). This corresponds to an average heat flux of about $q_o = 6$ and 8 mW/m^2 at the top of the ocean interface, assuming an ice shell thickness of 75–100 km. These two values lead to the pairs of parallel dashed colored lines in Fig. 10. For Titan's ocean, we assume the following parameters: gravity $g_0 = 1.35$ m/s^2, thermal diffusivity $\kappa = 1.3 \cdot 10^{-7}$ m^2/s and thermal expansivity $\alpha = 3.2 \cdot 10^{-4}$ K^{-1} (cf. Choukroun et al., 2010). Using these values and assuming $q_o = 6$–8 mW/m^2 and ocean thickness ranging between 90 and 450 km, the temperature difference across the ocean is between $4 \cdot 10^{-4}$ and $1.4 \cdot 10^{-3}$ K corresponding to Rayleigh numbers ranging between $3 \cdot 10^{19}$ (for $D = 90$ km and $q_o = 6$ mW/m^2 in the rapidly rotating case) and $1.3 \cdot 10^{23}$ (for $D = 450$ km and $q_o = 8$ mW/m^2 in the non-rotating case) (see Fig. 10).

Based on the above estimates Titan's ocean most likely falls in either the non-rotating or the transitional regimes. Of these two, the non-rotating regime has been studied extensively (for a summary see Gastine et al., 2016). Furthermore, as will be shown below (Section 5), observations suggest a significant latitudinal dependence of heat flux at the top of Titan's ocean with a fair degree of equatorial symmetry (as proposed by Soderlund et al., 2014, for Europa), a feature that the asymptotic non-rotating regime shall not produce. We thus focused our analysis (Section 2) on the less studied transitional regime, which is more promising in terms of latitudinal equatorially symmetric dynamics.

We obtained two main types of solutions (Section 3), characterized

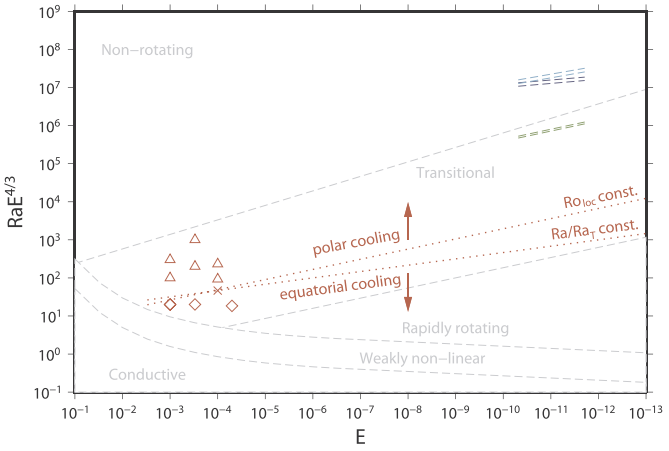

Fig. 10. Parameter space for convecting rotating flows in a spherical shell with the example of Titan. E is the Ekman number (Eq. (5)) and Ra is the Rayleigh number (Eq. (7)). $RaE^{4/3}$ is a measure of supercriticality of the Rayleigh number (Jones et al., 2000). The regime diagram obtained by Gastine et al. (2016) is reproduced by dashed grey lines. The parameter range corresponding to Titan's ocean is denoted by dashed colored lines. The estimated range for the Ekman number corresponds to endmember values for the ocean thickness D (Vance et al., 2018). Values for the Rayleigh number are based on three estimates of the temperature scale ΔT following the scaling for the non-rotating regime by Roche et al. (2010) (blue) and Gastine et al. (2015) (cyan) and the scaling for the rapidly rotating regime by Gastine et al. (2016) (green). For each of the three scaling laws, two lines correspond to the low and high heat flux values. The models presented in this study are denoted by red diamonds (equatorial cooling), red triangles (polar cooling) and red X (intermediate cooling). The two dotted red lines separating the equatorial and polar cooling regimes are given by constant values of the local convective Rossby number and Ra/Ra_T of intermediate case 8 respectively (see Table 2). For more details see text. (For interpretation of the references to color in this figure legend, the reader is referred to the web version of this article.)

by either larger outer boundary heat flux at low latitudes (which we term equatorial cooling and denote by red diamonds in Fig. 10) or by larger outer boundary heat flux at high latitudes (which we term polar cooling and denote by red triangles in Fig. 10). An intermediate cooling case with a more complicated flow pattern is denoted by red X in Fig. 10. As can be seen in Fig. 10, all our models fall within the transitional regime of Gastine et al. (2016). Constant values of the various Rossby numbers (see Section 2) which correspond to our intermediate case separate the equatorial and polar cooling models (see dotted red lines in Fig. 10).

The aspect ratio in our simulations (mostly 0.8) corresponds to a slightly thicker shell than the upper estimate of Vance et al. (2018). Note that they proposed internal structures that are not fully satisfactory in the case of Titan, since the compositional models for the rock component do not match the density of the interior model (Vance et al., 2018). More importantly, while our models and those of Gastine et al. (2016) are essentially similar (simulations of rotating convection of Boussinesq fluids), possible shifts of regime boundaries are expected between Titan's ocean dynamics and the simulations of Gastine et al. (2016). In the latter, gravity varies as r^{-2} and the ratio r_i/r_o is set to 0.6, whereas in our simulations gravity varies as r and the shell is thinner, both of which being probably more relevant choices for Titan's ocean. However, Mound and Davies (2017) found similar regime boundaries as Gastine et al. (2016) despite using different gravity profile, aspect ratio and boundary conditions. Whether this similarity holds for the non-accessible planetary parameters remains an open question.

5. Implications for the dynamics and structure of Titan's hydrosphere

Here, we compare the cooling regimes in our dynamical models to the heat flux anomalies at the top of Titan's ocean inferred from the analysis of topography and gravity data collected by the Cassini spacecraft (Kvorka et al., 2018). In Kvorka et al. (2018), Titan's topography (Lorenz et al., 2013) and gravity field (Iess et al., 2012) are interpreted with a viscoelastic flow model taking into account deflection of the ice/ocean interface and heat transport by thermal conduction through the ice shell including both heterogenous heat source due to tidal heating inside the ice shell and heat flux anomalies from the ocean. Two models of topography-dependent erosion and deposition are considered: one where erosion is neglected (NE, no erosion) and another where it is accounted for in a simple manner (E). The average heat flux values derived with such an approach depend on several rheological parameters for the ice among which the grain size, assumed uniform, and a cut-off maximum value. For simplicity, we adopt here the reference values favored by Kvorka et al. (2018) that were used in their Figs. 9 and 11.

Non-zonal effects might contribute to the global heat flux due to a heterogenous heat flux at the seafloor interface with a high-pressure ice mantle governing the specific dynamics of such a layer (Choblet et al., 2017b; Kalousová et al., 2018). Indeed, in the two models proposed by Kvorka et al. (2018), the non-zonal contributions are larger than the zonal contributions, by factors 1.9 (E) and 3.3 (NE). Here, we focus on the zonal part of the models of Kvorka et al. (2018) which may represent the internal dynamics in Titan's ocean.

Equatorial symmetry seems to dominate the zonal part of the heat flux models of Kvorka et al. (2018), with largest heat flux in the polar regions of both hemispheres (Fig. 11). To quantify this effect, we decomposed the zonal heat flux $q_o(\theta)$ to equatorially symmetric and anti-symmetric parts by

$$q_o^s(\theta) = \frac{q_o(\theta) + q_o(\pi - \theta)}{2} \tag{18}$$

and

$$q_o^a(\theta) = q_o(\theta) - q_o^s(\theta) \tag{19}$$

where the superscripts s and a denote symmetric and anti-symmetric

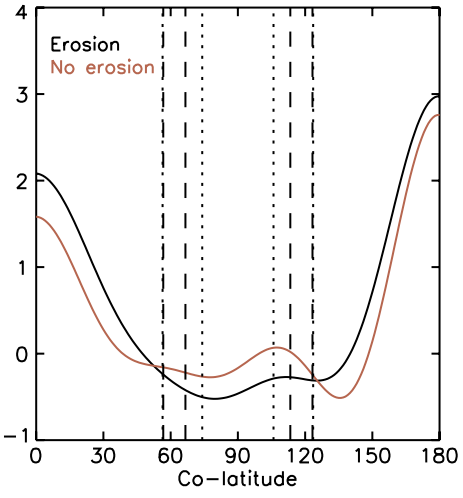

Fig. 11. Zonally-averaged heat flux in W/m^2 at the base of Titan's ice shell (Kvorka et al., 2018, see their Figs. 9 and 11) for models with (black) and without (red) erosion. Also indicated are plausible ranges for the latitude of the tangent cylinder at the base of the ice shell: vertical dashed lines based on Lefèvre et al. (2014) and vertical dotted lines based on Vance et al. (2018). (For interpretation of the references to color in this figure legend, the reader is referred to the web version of this article.)

parts respectively, and θ is in the northern hemisphere. Rms ratios of the equatorially anti-symmetric part to the equatorially symmetric part $||q_o^a||/||q_o^s||$ (where $||x||$ denotes the rms of x) for the two models yield values of 0.19 (E) and 0.37 (NE). We interpret these high levels of equatorial symmetry as a significant evidence that the rotating convecting dynamics highlighted in our simulations might play a key role in Titan's ocean.

The values of spatial heterogeneity for Titan's ocean are $< q_o^* >=$ 0.21 for the model without erosion (NE) and 0.30 for the model including erosion (E) (Kvorka et al., 2018). In our models, the values of spatial heterogeneity are $< q_o^* > \in [0.12 - 0.91]$ (Table 2), i.e. the inferred values for the spatial heterogeneity of Titan's ocean heat flux are well within the corresponding range in our simulations. Furthermore, if only values relevant for cases with polar cooling are considered among our simulations, the range narrows down to [0.12,0.26], in very good agreement with the values inferred for Titan in the models by Kvorka et al. (2018).

The latitudinal dependence of the heat flux at the top of the ocean indeed reveals a pronounced distribution of larger heat flux towards high latitudes (Fig. 11), i.e. polar cooling, for both the (E) and (NE) models. Following the scaling argument derived above (Figs. 8– 9 and Table 3), we anticipate that this noticeable feature could imply either a value of the local Rossby number Ro_{loc} larger than ~ 10 or alternatively a value of Ra/Ra_T larger than ~ 1, both applied for Titan's ocean. Given the relatively well constrained estimates for the Ekman number (cf. Section 4, $E \simeq 1.9 \cdot 10^{-12}$–$4.8 \cdot 10^{-11}$), the definition of Ro_{loc} (15) implies that the appropriate value for the Rayleigh number is larger than $2.0 \cdot 10^{17}$–$3.6 \cdot 10^{19}$. In contrast, for the same E range the definition of Ra/Ra_T (Eq. (16)) implies a somewhat lower range of values for the minimal Rayleigh number of $3.0 \cdot 10^{16} - 3.8 \cdot 10^{18}$. These lower bounds are in agreement with the range derived above of $Ra \simeq 10^{19}$–10^{25} (Section 4), but hardly puts a constraint on it. A potentially stronger insight into the Rayleigh number is derived considering that the polar cooling pattern indicates that Titan's ocean lies in the transitional regime depicted by Gastine et al. (2016) (Fig. 10), and not in the non-rotating regime since the latter should not involve latitudinal dependence of the heat flux. If the boundary between the two ($Ra < 100E^{-12/7}$) is directly applied to the case of Titan's ocean, its Rayleigh number is smaller than $4.9 \cdot 10^{19}$-$1.2 \cdot 10^{22}$, depending on the value for the Ekman number.

Finally, while the latitude at which the tangent cylinder intersects the outer boundary of Titan's ocean cannot be constrained from Fig. 11 without ambiguity, we also note that considering the ocean thickness ranges proposed in the literature (e.g. Lefèvre et al., 2014, Vance et al., 2018) allows to compute the ratio $< q_o >^{h/l}$ introduced in Eq. (11). For the thinnest shell considered by Vance et al. (2018) of $r_i/r_o = 0.96$, the latitude of the tangent cylinder is 16°, and the corresponding values for $< q_o >^{h/l}$ are 0.052 (E) and 0.016 (NE). For the thickest shell of $r_i/r_o = 0.83$, the latitude of the tangent cylinder is 34°, and the corresponding values for $< q_o >^{h/l}$ are 0.073 (E) and 0.025 (NE). All these are positive ratios, indicating polar cooling as expected. While the values for the model without erosion (NE) are slightly smaller than the range observed in our simulations with polar cooling ([0.06,0.16]), the values for the model with erosion (E) correspond to the lower end of this range. Together with its twice more pronounced equatorial symmetry, this may indicate that the model with erosion (E) is a better candidate for Titan's ice shell/ocean interaction. Note that the change of trend of the zonal heat flux based on the models of Kvorka et al. (2018) occurs at higher latitudes than the tangent cylinder (Fig. 11), in contrast to our self-consistent models in which the change of trend in the zonal heat flux appears at somewhat lower latitudes than the tangent cylinder (Fig. 7).

6. Discussion

In Earth's liquid outer core, which is a thick shell with an aspect ratio of 0.35, $E \ll 1$ and $Ro \ll 1$ (e.g. Olson, 2007), hence rapid rotation effects are thought to prevail. Outside the tangent cylinder, where the rotation and gravity vectors are nearly perpendicular, according to the Taylor-Proudman theorem the flow is expected to be invariant in the direction parallel to the rotation axis. This gives axial columns of fluid (e.g. Busse, 1970, Jault, 2008). Inside the tangent cylinder, where the rotation and gravity vectors are nearly parallel, the thermo-chemical wind balance gives spiraling flow with polar upwelling structures which are evident by observed dispersed magnetic flux (Olson and Aurnou, 1999) though in a somewhat non-trivial way (Cao et al., 2018). Competing rotation and convection effects determine the fluid dynamics in the shell. Close to the onset of convection when rotation effects dominate, columnar convection outside the tangent cylinder is more vigorous than thermal wind driven upwelling inside the tangent cylinder, resulting in equatorial cooling. Conversely, when convection effects dominate, these axial convective rolls are broken, convective plumes fill the tangent cylinder and the thermal wind driven polar upwelling results in polar cooling (Tilgner and Busse, 1997; Busse and Simitev, 2015). This effect is particularly significant with thin shells in which the tangent cylinder occupies a much larger surficial fraction of the outer boundary.

This rationale was recently explored in the context of thin shells which are applicable for the buried oceans of icy moons. Miquel et al. (2018) simulated the dynamics in a thin, rapidly rotating shell using 3D numerical models as well as a non-hydrostatic equatorial β-plane convection model. In both cases, they found that in the limit of rapid rotation (i.e. $E \ll 1$) convection is trapped at low latitudes and the peak heat flux appears at the equator (i.e. equatorial cooling). The latitudinal extent of the large equatorial heat flux is determined by ϵ/E where $\epsilon^2 = D/r_o$ (Miquel et al., 2018).

Our results show that the competition between rotation and convection is well captured by the Rossby number, as was previously proposed (Soderlund et al., 2014). We find that equatorial cooling prevails when the models are closer to the rapidly rotating regime, whereas polar cooling emerges when the models are closer to the non-rotating regime, in both cases within the transitional regime (Fig. 10) of Gastine et al. (2016). This parameter dependence of the latitudinal heat flux distribution is in agreement with previous studies (Tilgner and Busse, 1997; Busse and Simitev, 2015). For example, Busse and Simitev (2006) found in numerical dynamos with Earth-like geometry that increased rotation (i.e. lower E) gives more enhanced equatorial cooling. Likewise, Yadav et al. (2016) found in both rotating convection simulations and numerical dynamos that increased convection vigor (i.e. larger Ra) gives more enhanced polar cooling. Miquel et al. (2018) found in asymptotically thin shell, rapidly rotating models equatorially trapped convection that gives peak equatorial cooling. Guervilly and Cardin (2017) studied zonal flows and heat transport in a quasi-geostrophic model which allows accessing very low Ekman numbers. They found that the equatorial cooling pattern is further enhanced by the rapidly rotating quasi-geostrophic flows because the convective transport is perpendicular to the rotation axis. In contrast, early models with moderate rotation and convection vigor found mixed polar and equatorial cooling (Gilman, 1975, 1977), while Aurnou et al. (2008) found polar cooling in a rapidly rotating, strongly convecting simulation.

The key to reconcile these results may be the role of zonal flows. According to the Taylor-Proudman theorem, axial convective columns emerge in rapidly rotating fluids. These cylindrical flow structures are highly efficient in transporting heat in the equatorial region, hence the resulting equatorial cooling on approach to the rapidly rotating regime (e.g. Busse and Simitev, 2006, Guervilly and Cardin, 2017, Miquel et al., 2018, Yadav et al., 2016). However, increased rotation may give rise to stronger zonal flows that tend to diminish the equatorial heat flux, which may lead to polar cooling (Aurnou et al., 2008). Such strong zonal flows are especially prominent under free-slip boundary conditions (Aurnou et al., 2008; Yadav et al., 2016) but may also emerge with no-slip boundary conditions. The zonal flow exhibits non-monotonic dependence on the Rossby number (Yadav et al., 2016) which may

then explain these two contradicting parameter dependences of the outer boundary heat flux pattern. Additional complications may arise due to dependences on e.g. the shell thickness and the Prandtl number.

In the context of Titan's buried ocean, a new independent constraint is brought from the inferred heat flux models of Kvorka et al. (2018). These models clearly indicate that polar cooling prevails at the top of Titan's ocean (Fig. 11). Assuming that this is true, we envision two possible interpretations. According to our models, Titan's ocean is at the transitional regime close to the non-rotating regime with relatively strong convection. In contrast, according to the model of Aurnou et al. (2008), convection in Titan's ocean would be relatively weak and the dynamics would then be dominated by rotational effects, but strong zonal flows diminish the equatorial heat flux.

It is worth noting that the regime diagram (Fig. 10) of Gastine et al. (2016) was obtained using a fixed shell aspect ratio of 0.6 and fixed ΔT boundary conditions. Different thermal boundary conditions (i.e. prescribed heat flux at one or both boundaries) or different shell thicknesses would likely require some updating of the scaling laws separating the different flow regimes. For example, our cases 1 and 2 have the same control parameters (hence overlap in Fig. 10) but different shell thicknesses (Table 2). Although both cases give equatorial cooling, the amplitude of $< q_o >^{h/l}$ in case 2 with the thinner shell is twice smaller (Table 3), suggesting that (for given control parameters) a thinner shell favors polar cooling. In that respect, replacing Ra by the convective power, which accounts for both the thermal boundary conditions and the shell geometry (Aubert et al., 2009), could be more appropriate. Other phenomena (e.g. compositional effects) might also induce biases. Nevertheless, qualitatively the diagram in Fig. 10 may provide a useful guidance for comparing numerical models and natural bodies.

Our choice of isothermal and impermeable boundary conditions is not necessarily the most physically relevant. The outer boundary of the ocean corresponds to a phase change. So does the inner boundary in the case where high-pressure polymorphs of ice form a layer beneath. In a situation where isothermal conditions are applied to mimic the melting-freezing boundary, the choice of a non-penetrative velocity condition is questionable. Alternatively, slowly evolving convection in the surrounding solid ice layers may affect the latitudinal variations in heat flux at the top of the ocean. Dynamics in the high-pressure ice mantle below the ocean may give heterogenous heat flux at the seafloor (Choblet et al., 2017b; Kalousová et al., 2018), whereas solid-state convection in the ice shell above can induce significant temperature anomalies, even more so if latitudinal variation in surface insolation induces planetary scale convective features with polar downwelling and equatorial upwelling (Weller et al., in press). If the surrounding ice shells can indeed support slowly varying large lateral temperature variations, then the more appropriate thermal boundary conditions for the ocean could be prescribed heterogeneous flux.

While our main planetary target here is Titan, other ocean worlds would likely correspond to other regions in the regime diagram. Considering an average value for the ocean thickness of 40 km, Enceladus displays an Ekman number and geometry comparable to Titan's: $E \simeq 2.2 \cdot 10^{-11}$ and $r_i/r_o = 0.83$. A plausible range for Enceladus' ocean Rayleigh number involves however significantly lower values than Titan's: $Ra \simeq 5 \cdot 10^{17} - 10^{21}$. This would in theory imply that the appropriate range for Enceladus' ocean lies exclusively in the transitional regime with equatorial cooling as a possibility. However, because Enceladus' ice shell is more than three times thicker near the equator than near the poles (Beuthe et al., 2016; Čadek et al., 2016; Le Gall et al., 2017) and internal heating in the ice shell is negligible (Čadek et al., 2019), equatorial cooling is unlikely for its ocean. Furthermore, the actual heat flux pattern at the top of Enceladus' ocean may be dominated by polar cooling due to forcing coming from its core (Choblet et al., 2017a). Overall, various complexities (non-spherical container, strongly heterogeneous bottom heat flux) should be considered for some planetary objects. Given the variety of sizes and orbital characteristics, distinct dynamical regimes are expected for subsurface oceans of icy moons.

As acknowledged by Kvorka et al. (2018), inaccurate topography and gravity measurements render their derived heat flux models uncertain. It is therefore probably premature to draw definite conclusions from the comparison exercise between Titan's heat flux inferred from observations and our simulated heat flux at the top of the shell. Nevertheless, we consider that the overall agreement in terms of pattern and amplitude is encouraging for both approaches. This also highlights the importance of future geophysical observations by space missions which may further constrain the dynamics of deep oceans.

Acknowledgments

This work acknowledges the financial support from Région Pays de la Loire, project GeoPlaNet (convention N° 2016-10982). We also acknowledge support from CNES JUICE and Europa Clipper. We are grateful to Krista Soderlund and Thomas Gastine for insightful discussions that enriched this paper. We thank two anonymous reviewers for constructive comments that improved the paper.

References

Amit, H., Choblet, G., 2009. Mantle-driven geodynamo features — effects of post-Perovskite phase transition. Earth. Planet. Space. 61, 1255–1268.
Amit, H., Choblet, G., Olson, P., Monteux, J., Deschamps, F., Langlais, B., Tobie, G., 2015. Towards more realistic core-mantle boundary heat flux patterns: a source of diversity in planetary dynamos. Prog. Earth Planet. Sci. 2:26 https://doi.org/10.1186/s40645-015-0056-3.
Aubert, J., Amit, H., Hulot, G., 2007. Detecting thermal boundary control in surface flows from numerical dynamos. Phys. Earth Planet. Inter. 160, 143–156.
Aubert, J., Amit, H., Hulot, G., Olson, P., 2008. Thermo-chemical wind flows couple Earth's inner core growth to mantle heterogeneity. Nature 454, 758–761.
Aubert, J., Gastine, T., Fournier, A., 2017. Spherical convective dynamos in the rapidly rotating asymptotic regime. J. Fluid. Mech. 813, 558–593.
Aubert, J., Labrosse, S., Poitou, C., 2009. Modelling the paleo-evolution of the geodynamo. Geophys. J. Int. 179, 1414–1428.
Aurnou, J., Heimpel, M., Allem, L., King, E., Wicht, J., 2008. Convective heat transfer and the pattern of thermal emission on the gas giants. Geophys. J. Int. 173, 793–801.
Baland, R.-M., Tobie, G., Lefèvre, A., Van Hoolst, T., 2014. Titan's internal structure inferred from its gravity field, shape, and rotation state. Icarus 237, 29–41.
Baland, R.-M., Van Hoolst, T., Yseboodt, M., Karatekin, O., 2011. Titan's obliquity as evidence of a subsurface ocean? Astronom. Astrophys. 530, A141.
Béghin, C., Randriamboarison, O., Hamelin, M., Karkoschka, E., Sotin, C., Whitten, R.C., Berthelier, J.-J., Grard, R., Sim oes, F., 2012. Analytic theory of Titan's Schumann resonance: constraints on ionospheric conductivity and buried water ocean. Icarus 218(2), 1028–1042.
Béghin, C., Sotin, C., Hamelin, M., 2010. Titan's native ocean revealed beneath some 45 km of ice by a Schumann-like resonance. Comp. Rend. Geosci. 342, 425–433.
Beuthe, M., Rivoldini, A., Trinh, A., 2016. Enceladus's and Dione's floating ice shells supported by minimum stress isostasy. Geophys. Res. Lett. 43(19), 10088–10096.
Busse, F., 1970. Thermal instabilities in rapidly rotating systems. J. Fluid Mech. 44, 441–460.
Busse, F., Simitev, R., 2006. Parameter dependences of convection-driven dynamos in rotating spherical fluid shells. Geophys. Astrophys. Fluid Dyn. 100, 341–361.
Čadek, O., Souček, O., Běhounková, M., Choblet, G., Tobie, G., Hron, J., 2019. Long-term stability of Enceladus uneven ice shell. Icarus 319, 476–484.
Čadek, O., Tobie, G., Van Hoolst, T., Massé, M., Choblet, G., Lefèvre, A., Mitri, G., Baland, R.-M., Běhounková, M., Bourgeois, O., et al., 2016. Enceladus's internal ocean and ice shell constrained from Cassini gravity, shape, and libration data. Geophys. Res. Lett. 43, 5653–5660.
Cao, H., Yadav, R.K., Aurnou, J., 2018. Geomagnetic polar minima do not arise from steady meridional circulation. Proc. Nat. Acad. Sci. 115 (44), 11186–11191.
Choblet, G., Tobie, G., Sotin, C., Běhounková, M., Čadek, O., Postberg, F., Souček, O., 2017. Powering prolonged hydrothermal activity inside Enceladus. Nature Astro. 1 (12), 841.
Choblet, G., Tobie, G., Sotin, C., Kalousova, K., Grasset, O., 2017. Heat transport in the high-pressure ice mantle of large icy moon. Icarus 285, 252–262.
Choukroun, M., Grasset, O., Tobie, G., Sotin, C., 2010. Stability of methane clathrate hydrates under pressure: influence on outgassing processes of methane on Titan. Icarus 205, 581–593.
Dormy, E., Soward, A.M., Jones, C.A., Jault, D., Cardin, P., 2004. The onset of thermal convection in rotating spherical shells. J. Fluid Mech. 501, 43–70.
Dziewonski, A.M., Anderson, D.L., 1981. Preliminary reference Earth model. Phys. Earth Planet. Inter. 25, 297–356.
Gabasova, L.R., Tobie, G., Choblet, G., 2018. Compaction-driven evolution of Pluto's rocky core: implications for water-rock interactions. In: *Ocean Worlds*, 20185.
Gastine, T., Wicht, J., Aubert, J., 2016. Scaling regimes in spherical shell rotating convection. J. Fluid. Mech. 808, 690–732.

Gastine, T., Wicht, J., Aurnou, J., 2015. Turbulent Rayleigh-béNard convection in spherical shells. J. Fluid Mech. 778, 721–764.
Gilman, P., 1975. Linear simulations of Boussinesq convection in a deep rotating spherical shell. J. Atmos. Sci. 32, 1331–1352.
Gilman, P., 1977. Nonlinear dynamics of Boussinesq convection in a deep rotating shellI. Geophys. Astrophys. Fluid Dyn. 8, 93–135.
Glatzmaier, G., 2002. Geodynamo simulations: how realistic are they? Annu. Rev. Earth Planet. Sci. Lett. 30, 237–257.
Goodman, J.C., Collins, G.C., Marshall, J., Pierrehumbert, R.T., 2004. Hydrothermal plume dynamics on Europa: implications for chaos formation. J. Geophys. Res. 109 (E3).
Grasset, O., Dougherty, M., Coustenis, A., Bunce, E., Erd, C., Titov, D., Blanc, M., Coates, A., Drossart, P., Fletcher, L., et al., 2013. Jupiter icy moons explorer (JUICE): an ESA mission to orbit Ganymede and to characterise the Jupiter system. Plan. Space Sci. 78, 1–21.
Guervilly, C., Cardin, P., 2017. Multiple zonal jets and convective heat transport barriers in a quasi-geostrophic model of planetary cores. Geophys. J. Int. 211, 455–471.
Hauck, S.A., Mazarico, E., Padovan, S., Peale, S.J., 2018. Mercury's internal structure. In: Solomon, S.C., Anderson, B.J., Nittler, L.R. (Eds.), Mercury — The View after MESSENGER. .
Heimpel, M., Evans, M., 2013. Testing the geomagnetic dipole and reversing dynamo models over Earth's cooling history. Phys. Earth Planet. Inter. 224, 124–131.
Hemingway, D., Iess, L., Tajeddine, R., Tobie, G., 2018. The interior of Enceladus. In: Schenk, P.M.e.a. (Ed.), *Enceladus and the Icy Moons of Saturn*. Univ. of Arizona, Tucson.
Hsu, H.-W., Postberg, F., Sekine, Y., Shibuya, T., Kempf, S., Horanyi, M., Juhász, A., Altobelli, N., Suzuki, K., Masaki, Y., Kuwatani, T., Tachibana, S., Sirono, S.-I., Moragas-Klostermeyer, G., Srama, R., 2015. Ongoing hydrothermal activities within Enceladus. Nature 519, 207–210.
Hsu, H.-W., Schmidt, J., Kempf, S., Postberg, F., Moragas-Klostermeyer, G., Seiß, M., Hoffmann, H., Burton, M., Ye, S., Kurth, W.S., Horányi, M., Khawaja, N., Spahn, F. e. a., 2018. In situ collection of dust grains falling from Saturn's rings into its atmosphere. Science 362. https://doi.org/10.1126/science.aat3185.
Iess, L., Jacobson, R., Ducci, M., Stevenson, D., Lunine, J.I., Armstrong, J.W., Asmar, S., Racioppa, P., Rappaport, N.J., Tortora, P., 2012. The tides of Titan. Science 337, 457–459.
Iess, L., Rappaport, N.J., Jacobson, R.A., Racioppa, P., Stevenson, D.J., Tortora, P., Armstrong, J.W., Asmar, S.W., 2010. Gravity field, shape, and moment of inertia of Titan. Science 327, 1367–1369.
Jault, D., 2008. Axial invariance of rapidly varying diffusionless motions in the Earth's core interior. Geophys. J. Int. 166, 67–76.
Jones, C., Soward, A., Mussa, A., 2000. The onset of thermal convection in a rapidly rotating sphere. J. Fluid Mech. 405, 157–179.
Kalousová, K., Sotin, C., Choblet, G., Tobie, G., Grasset, O., 2018. Two-phase convection in Ganymede's high-pressure ice layer-implications for its geological evolution. Icarus 299, 133–147.
Khurana, K.K., Kivelson, M.G., Russell, C.T., 2002. Searching for liquid water in Europa by using surface observatories. Astrobiology 2(1), 93–103.
Kirk, R., Stevenson, D., 1987. Thermal evolution of a differentiated Ganymede and implications for surface features. Icarus 69(1), 91–134.
Kivelson, M., Khurana, K., 2002. The permanent and inductive magnetic moments of Ganymede. Icarus 157 (2), 507–522.
Kvorka, J., Čadek, O., Tobie, G., Choblet, G., 2018. Does Titan's long-wavelength topography contain information about subsurface ocean dynamics? Icarus 310, 149–164.
Le Gall, A., Leyrat, C., Janssen, M.A., Choblet, G., Tobie, G., Bourgeois, O., Lucas, A., Sotin, C., Howett, C., Kirk, R., et al., 2017. Thermally anomalous features in the subsurface of Enceladus's south polar terrain. Nature Astro. 1 (4), 0063.
Lefèvre, A., Tobie, G., Choblet, G., Čadek, O., 2014. Structure and dynamics of Titan's outer icy shell constrained from Cassini data. Icarus 237, 16–28.
Ligier, N., Poulet, F., Carter, J., Brunetto, R., Gourgeot, F., 2016. Vlt/Sinfoni observations of Europa: new insights into the surface composition. Astronom. J. 151:163.
Lorenz, R.D., Stiles, B.W., Aharonson, O., Lucas, A., Hayes, A.G., Kirk, R.L., Zebker, H.A., Turtle, E.P., Neish, C.D., Stofan, E.R., et al., 2013. A global topographic map of Titan. Icarus 225 (1), 367–377.
McCord, T.B., Teeter, G., Hansen, G.B., Sieger, M.T., Orlando, T.M., 2002. Brines exposed to Europa surface conditions. J. Geophys. Res. 107 (E1), 5004.
Miquel, B., Xie, J.-H., Featherstone, N., Julien, K., Knobloch, E., 2018. Equatorially trapped convection in a rapidly rotating shallow shell. Phys. Rev. Fluids 3, 053–801.
Mitri, G., Meriggiola, R., Hayes, A., Lefèvre, A., Tobie, G., Genova, A., Lunine, J.I., Zebker, H., 2014. Shape, topography, gravity anomalies and tidal deformation of Titan. Icarus 236, 169–177.
Nimmo, F., Pappalardo, R., 2016. Ocean worlds in the outer solar system. J. Geophys. Res. 121(8), 1378–1399.
Ojakangas, G.W., Stevenson, D.J., 1989. Thermal state of an ice shell on Europa. Icarus 81(2), 220–241.
Olson, P., 2007. Overview. In: Olson, P. (Ed.), *Treatise on Geophysics*, 8. Elsevier Science.
Olson, P., Aurnou, J., 1999. A polar vortex in the Earth's core. Nature 402, 170–173.
Olson, P., Christensen, U., 2002. The time averaged magnetic field in numerical dynamos with nonuniform boundary heat flow. Geophys. J. Int. 151, 809–823.
Phillips, C.B., Pappalardo, R.T., 2014. Europa Clipper mission concept: exploring Jupiter's ocean moon. Eos Trans. AGU 95(20), 165–167.
Postberg, F., Kempf, S., Schmidt, J., Brilliantov, N., Beinsen, A., Abel, B., Buck, U., Srama, R., 2009. Sodium salts in E-ring ice grains from an ocean below the surface of Enceladus. Nature 459 (7250), 1098.
Postberg, F., Schmidt, J., Kempf, S., Hillier, S., Srama, R., 2011. A salt-water reservoir as the source of a compositionally stratified plume on Enceladus. Nature 474, 620–622.
Roche, P.-E., Gauthier, F., Kaiser, R., Salort, J., 2010. On the triggering of the ultimate regime of convection. New J. Phys. 12, 085014.
Saur, J., Duling, S., Roth, L., Jia, X., Strobel, D.F., Feldman, P.D., Christensen, U.R., Retherford, K.D., McGrath, M.A., Musacchio, F., et al., 2015. The search for a subsurface ocean in Ganymede with Hubble space telescope observations of its auroral ovals. J. Geophys. Res. 120 (3), 1715–1737.
Schaeffer, N., 2013. Efficient spherical harmonic transforms aimed at pseudo-spectral numerical simulations. Geochem. Geophys. Geosyst. 14, 751–758.
Schaeffer, N., Jault, D., Nataf, H.-C., Fournier, A., 2017. Turbulent geodynamo simulations: a leap towards Earth's core. Geophys. J. Int. 211, 1–29.
Soderlund, K.M., Schmidt, B.E., Wicht, J., Blankenship, D.D., 2014. Ocean-driven heating of Europa's icy shell at low latitudes. Nature Geosci. 7, 16–19.
Tajeddine, R., Rambaux, N., Lainey, V., Charnoz, S., Richard, A., Rivoldini, A., Noyelles, B., 2014. Constraints on Mimas' interior from Cassini ISS libration measurements. Science 346(6207), 322–324.
Taylor, G., 1917. Motion of solids in fluids when the flow is not irrotational. Proc. R. Soc. Lond. A. 93, 92–113.
Thomas, P., Tajeddine, R., Tiscareno, M., Burns, J., Joseph, J., Loredo, T., Helfenstein, P., Porco, C., 2016. Enceladus' measured physical libration requires a global subsurface ocean. Icarus 264, 37–47.
Thomson, R.E., Delaney, J.R., 2001. Evidence for a weakly stratified European ocean sustained by seafloor heat flux. J. Geophys. Res. 106(E6), 12355–12365.
Tilgner, A., Busse, F.H., 1997. Finite-amplitude convection in rotating spherical fluid shells. J. Fluid Mech. 332, 359–376.
Tobie, G., Lunine, J.I., Sotin, C., 2006. Episodic outgassing as the origin of atmospheric methane on Titan. Nature 440, 61–64.
Vance, S., Brown, J., 2005. Layering and double-diffusion style convection in Europa's ocean. Icarus 177(2), 506–514.
Vance, S., Goodman, J., 2009. Oceanography of an ice-covered moon. Europa 459–484.
Vance, S.D., Panning, M.P., Stähler, S., Cammarano, F., Bills, B.G., Tobie, G., Kamata, S., Kedar, S., Sotin, C., Pike, W.T., et al., 2018. Geophysical investigations of habitability in ice-covered ocean worlds. J. Geophys. Res. 123 (1), 180–205.
Vidal, J., Schaeffer, N., 2015. Quasi-geostrophic modes in the Earth's fluid core with an outer stably stratified layer. Geophys. J. Int. 202, 2182–2193.
Weller, M.B., Fuchs, L., Becker, T.W., Soderlund, K.M., 2019. Convection in thin shells of icy satellites: effects of latitudinal surface temperature variations. J. Geophys. Res. 124, 2029–2053.
Wicht, J., 2002. Inner-core conductivity in numerical dynamo simulations. Phys. Earth Planet. Inter. 132, 281–302.
Yadav, R., Gastine, T., Christensen, U., Duarte, L., Reiners, A., 2016. Effect of shear and magnetic field on the heat-transfer efficiency of convection in rotating spherical shells. Geophys. J. Int. 204, 1120–1133.
Zhang, K., Jones, C.A., 1993. The influence of Ekman boundary layers on rotating convection. Geophys. Astrophys. Fluid Dyn. 71, 145–162.
Zimmer, C., Khurana, K.K., Kivelson, M.G., 2000. Subsurface oceans on Europa and Callisto: constraints from Galileo magnetometer observations. Icarus 147(2), 329–347.